



**HAL**  
open science

## Sparse sampling, galaxy bias, and voids

P. M. Sutter, Guilhem Lavaux, Nico Hamaus, Benjamin D. Wandelt, David H. Weinberg, Michael S. Warren

► **To cite this version:**

P. M. Sutter, Guilhem Lavaux, Nico Hamaus, Benjamin D. Wandelt, David H. Weinberg, et al.. Sparse sampling, galaxy bias, and voids. *Monthly Notices of the Royal Astronomical Society*, 2014, 442, pp.462-471. 10.1093/mnras/stu893 . insu-03645359

**HAL Id: insu-03645359**

**<https://insu.hal.science/insu-03645359>**

Submitted on 24 Apr 2022

**HAL** is a multi-disciplinary open access archive for the deposit and dissemination of scientific research documents, whether they are published or not. The documents may come from teaching and research institutions in France or abroad, or from public or private research centers.

L'archive ouverte pluridisciplinaire **HAL**, est destinée au dépôt et à la diffusion de documents scientifiques de niveau recherche, publiés ou non, émanant des établissements d'enseignement et de recherche français ou étrangers, des laboratoires publics ou privés.

# Sparse sampling, galaxy bias, and voids

P. M. Sutter,<sup>1,2,3,4★</sup> Guilhem Lavaux,<sup>1,2,5,6,7</sup> Nico Hamaus,<sup>1,2,4</sup>  
Benjamin D. Wandelt,<sup>1,2,4,8</sup> David H. Weinberg<sup>3,9</sup> and Michael S. Warren<sup>10</sup>

<sup>1</sup>*Sorbonne Universités, UPMC Univ. Paris 06, UMR7095, Institut d'Astrophysique de Paris, F-75014 Paris, France*

<sup>2</sup>*CNRS, UMR7095, Institut d'Astrophysique de Paris, F-75014 Paris, France*

<sup>3</sup>*Center for Cosmology and Astro-Particle Physics, Ohio State University, Columbus, OH 43210, USA*

<sup>4</sup>*Department of Physics, University of Illinois at Urbana-Champaign, Urbana, IL 61801, USA*

<sup>5</sup>*Department of Physics & Astronomy, University of Waterloo, Waterloo, ON N2L 3G1, Canada*

<sup>6</sup>*Perimeter Institute for Theoretical Physics, Waterloo, ON N2L 2Y5, Canada*

<sup>7</sup>*Canadian Institute for Theoretical Astrophysics, 60 St. George St, Toronto, ON M5S 3H8, Canada*

<sup>8</sup>*Department of Astronomy, University of Illinois at Urbana-Champaign, Urbana, IL 61801, USA*

<sup>9</sup>*Department of Astronomy, Ohio State University, Columbus, OH 43210, USA*

<sup>10</sup>*Theoretical Division, Los Alamos National Laboratory, Los Alamos, NM 87545, USA*

Accepted 2014 May 3. Received 2014 May 3; in original form 2013 September 19

## ABSTRACT

To study the impact of sparsity and galaxy bias on void statistics, we use a single large-volume, high-resolution  $N$ -body simulation to compare voids in multiple levels of subsampled dark matter, halo populations, and mock galaxies from a halo occupation distribution model tuned to different galaxy survey densities. We focus our comparison on three key observational statistics: number functions, ellipticity distributions, and radial density profiles. We use the hierarchical tree structure of voids to interpret the impacts of sampling density and galaxy bias, and theoretical and empirical functions to describe the statistics in all our sample populations. We are able to make simple adjustments to theoretical expectations to offer prescriptions for translating from analytics to the void properties measured in realistic observations. We find that sampling density has a much larger effect on void sizes than galaxy bias. At lower tracer density, small voids disappear and the remaining voids are larger, more spherical, and have slightly steeper profiles. When a proper lower mass threshold is chosen, voids in halo distributions largely mimic those found in galaxy populations, except for ellipticities, where galaxy bias leads to higher values. We use the void density profile of Hamaus et al. to show that voids follow a self-similar and universal trend, allowing simple translations between voids studied in dark matter and voids identified in galaxy surveys. We have added the mock void catalogues used in this work to the Public Cosmic Void Catalog at <http://www.cosmicvoids.net>.

**Key words:** methods: data analysis – methods: numerical – cosmology: theory – large-scale structure of Universe.

## 1 INTRODUCTION

The large, underdense structures that fill up most of the volume of the universe – are a unique and potentially powerful cosmological probe (Thompson & Gregory 2011). Their size and shape distributions are sensitive to the nature of dark energy (e.g. Biswas, Alizadeh & Wandelt 2010; Bos et al. 2012; Li, Zhao & Koyama 2012; Shoji & Lee 2012; Jennings, Li & Hu 2013), their internal dynamics are strongly altered by fifth forces and modified gravity (e.g. Li & Zhao 2009; Clampitt, Cai & Li 2013; Spolyar, Sahlén & Silk 2013), and the integrated Sachs–Wolfe effect offers constraints on cosmological parameters (Thompson & Vishniac 1987;

Ilic, Langer & Douspis 2013; Planck Collaboration 2013). Their statistical isotropy means that we can use stacked voids as a standard sphere for an Alcock–Paczynski test (Ryden 1995; Lavaux & Wandelt 2012; Sutter et al. 2012b). Additionally, we may use voids to test for the existence of primordial magnetic fields (Taylor, Vovk & Neronov 2011; Beck et al. 2013) and study the effects of environment on galaxy evolution (Gottlober et al. 2003; Ferreras & Pasquali 2011; Ceccarelli et al. 2012).

Researchers typically use analytical calculations and  $N$ -body dark matter simulations to predict and understand various void properties, such as number functions (Sheth & van de Weygaert 2004; Furlanetto & Piran 2006; Paranjape, Lam & Sheth 2012; Achitouv, Neyrinck & Paranjape 2013; Jennings et al. 2013), radial density profiles (Fillmore & Goldreich 1984; Dubinski et al. 1993; Benson et al. 2003; Colberg et al. 2005; Ceccarelli et al. 2006), and

\* E-mail: [sutter2@iap.fr](mailto:sutter2@iap.fr)

ellipticities (Lavaux & Wandelt 2010; Bos et al. 2012; Shoji & Lee 2012). However, absent direct measurements of dark matter underdensities the only way to infer the characteristics of voids is with large galaxy redshift the only way to infer the characteristics of voids is with large galaxy redshift surveys (Pan et al. 2012; Sutter et al. 2012a). These galaxy populations are sparse, biased tracers of the underlying dark matter density field, which can potentially impact void statistics.

There has already been some work to make the connection between galaxy and dark matter voids: Furlanetto & Piran (2006) and Jennings et al. (2013) made parameter adjustments to the excursion set formalism of Sheth & van de Weygaert (2004) to account for void finding in galaxy populations, Ryden & Melott (1996) compared voids in real and redshift space, Tinker & Conroy (2009) looked at the impacts of the biasing of different galaxy populations, and Schmidt, Ryden & Melott (2001) and Colberg et al. (2005) made early assessments of the effects of different sparsity levels on void reconstruction. When attempting to *predict* void statistical properties, most authors find voids within the halo distribution, not a mock galaxy population (e.g. Bos et al. 2012; Jennings et al. 2013). We will discuss the validity of this assumption below. When attempting to *match* observed void statistics, authors typically turn to semi-analytic modelling (SAM; De Lucia 2009) to generate mock galaxy populations (Benson et al. 2003; Padilla, Ceccarelli & Lambas 2005; Ceccarelli et al. 2006; Pan et al. 2012; Tavasoli, Vasei & Mohayaee 2013).

While it may be possible to link galaxy voids to dark matter voids on a one-by-one basis, this is very difficult due to the complex internal hierarchical structure of voids (Aragon-Calvo & Szalay 2013; Sutter et al. 2014). Instead, in this work, we take a holistic approach and offer general prescriptions to translate from dark matter voids to galaxy voids by examining voids in different tracer populations sourced from the same cosmological simulation. We focus on three key void observables: number functions, ellipticity distributions, and radial density profiles. We take theoretical and empirically derived fitting functions and adjust their parameters to move smoothly among the different populations.

We begin in Section 2 with our simulation setup, our process for generating mock galaxy populations, and our void finding algorithm. Next, in Section 3, we use the hierarchical tree structure of voids to examine the consequences of reducing the tracer density and introducing galaxy bias. Section 4 discusses the changes to number functions, ellipticity distributions, and radial density profiles. Finally, we conclude in Section 5 with a discussion of consequences for interpreting voids in galaxy redshift surveys and comments on future work.

## 2 NUMERICAL APPROACH

### 2.1 Simulations and mocks

We source all samples and mock catalogues in this work from a single  $\Lambda$  cold dark matter  $N$ -body simulation. We use the 2HOT code, an adaptive treecode  $N$ -body method whose operation count scales as  $N \log N$  in the number of particles (Warren 2013). Accuracy and error behaviour have been improved significantly for cosmological volumes through the use of a technique to subtract the uniform background density, as well as using a compensating smoothing kernel for small-scale force softening (Dehnen 2001). We use a standard symplectic integrator (Quinn et al. 1997) and an efficient implementation of periodic boundary conditions using a high-order ( $p = 8$ ) multipole local expansion. We adjust the error tolerance parameter to limit absolute errors to 0.1 per cent of the rms peculiar

acceleration. As an example, a complete  $4096^3$  particle simulation requires about 120 wall-clock hours using 12 000 CPU cores. Initial conditions were generated using a power spectrum calculated with CLASS (Blas, Lesgourgues & Tram 2011) and realized with a modified version of 2LPTIC (Croce, Pueblas & Scoccimarro 2006).

This particular simulation assumed WMAP 7-yr cosmological parameters (Komatsu et al. 2011). The box size was  $1 h^{-1}$  Gpc on a side and contained  $1024^3$  particles, giving a particle mass resolution of  $7.36 \times 10^{10} h^{-1} M_{\odot}$ . All analysis in this work used a single snapshot at  $z = 0$ . For the dark matter analysis, we take successive random subsamples of the particles to achieve tracer densities of  $10^{-2}$ ,  $4 \times 10^{-3}$ , and  $3 \times 10^{-4}$  particles per cubic  $h^{-1}$  Mpc. These samples are labelled as *DM Full*, *DM Dense*, and *DM Sparse*, respectively.

We use the ROCKSTAR halo finder (Behroozi, Wechsler & Wu 2013), a six-dimensional phase-space plus time halo finder, to identify spherical overdensity (SO) haloes at 200 times the background density. We use the default ROCKSTAR parameters, except for requiring strict SO masses which includes unbound particles and particles which may exist outside of the FOF group for the halo. We use the halo catalogue both for using the halo positions as a set of tracers for void finding and as inputs for the halo occupation distribution (HOD) modelling. We take two halo populations: one, labelled *Halo Dense*, which uses all haloes down to the minimum resolvable halo mass of  $1.47 \times 10^{12} h^{-1} M_{\odot}$  (20 particles), and the other, labelled *Halo Sparse*, which only includes haloes above  $1.2 \times 10^{13} h^{-1} M_{\odot}$ . These samples do not have exactly the same densities as the HOD mocks below; rather, we use these two thresholds to approximate the minimum mass used in the HOD distribution of central galaxies, thereby allowing us to compare voids found in haloes to those found in galaxy populations.

We produce galaxy catalogues from the above halo population using the code described in Tinker, Weinberg & Zheng (2006) and the HOD model described in Zheng, Coil & Zehavi (2007). HOD modelling assigns central and satellite galaxies to a dark matter halo of mass  $M$  according to a parametrized distribution. In the case of the Zheng et al. (2007) parametrization, the mean number of central galaxies is given by

$$\langle N_{\text{cen}}(M) \rangle = \frac{1}{2} \left[ 1 + \text{erf} \left( \frac{\log M - \log M_{\text{min}}}{\sigma_{\log M}} \right) \right] \quad (1)$$

and the mean number of satellites is given by

$$\langle N_{\text{sat}}(M) \rangle = \langle N_{\text{cen}}(M) \rangle \left( \frac{M - M_0}{M'_1} \right)^{\alpha}, \quad (2)$$

where  $M_{\text{min}}$ ,  $\sigma_{\log M}$ ,  $M_0$ ,  $M'_1$ , and  $\alpha$  are free parameters that must be fitted to a given survey. The probability distribution of central galaxies is a nearest-integer distribution (i.e. all haloes above a given mass threshold host a central galaxy), and satellites follow Poisson statistics.

Using the above model, we generate two mock catalogues. One catalogue is matched to the number density and clustering of the SDSS DR9 CMASS galaxy sample (Dawson et al. 2013) using the parameters found by Manera et al. (2013) ( $\sigma_{\log M} = 0.596$ ,  $M_0 = 1.2 \times 10^{13} h^{-1} M_{\odot}$ ,  $M'_1 = 10^{14} h^{-1} M_{\odot}$ ,  $\alpha = 1.0127$ , and  $M_{\text{min}}$  chosen to fit the mean number density). We call this sample *HOD Sparse* since we are using it to represent a relatively low-resolution galaxy sample with density  $3 \times 10^{-4}$  particles per cubic  $h^{-1}$  Mpc. Our second catalogue, named *HOD Dense*, is matched to the SDSS DR7 main sample (Strauss et al. 2002) at  $z < 0.1$  using one set of parameters found by Zehavi et al. (2011) ( $\sigma_{\log M} = 0.21$ ,  $M_0 = 6.7 \times 10^{13} h^{-1} M_{\odot}$ ,  $M'_1 = 2.8 \times 10^{13} h^{-1} M_{\odot}$ ,  $\alpha = 1.12$ ). While our simulation does not quite have sufficient resolution to

have enough small haloes to fully capture the density of this survey, we will still use it to represent relatively high-resolution galaxy samples. The density here,  $4 \times 10^{-3}$  particles per cubic  $h^{-1}$  Mpc, is roughly a factor of 2 lower than the full DR7 density at  $z < 0.1$ .

## 2.2 Void finding

We identify voids with a modified version of ZOBOV (Neyrinck 2008; Lavaux & Wandelt 2012; Sutter et al. 2012a). ZOBOV creates a Voronoi tessellation of the tracer particle population, and uses the watershed transform to group Voronoi cells into zones and voids (Platen, van de Weygaert & Jones 2007). The watershed transform identifies catchment basins as the cores of voids and ridgelines, which separate the flow of water, as the boundaries of voids. The watershed transform naturally builds a nested hierarchy of voids (Bos et al. 2012; Lavaux & Wandelt 2012), and for the purposes of this work – with the exception of Section 3, where we explicitly discuss the void hierarchy – we will only examine *root* voids, which are voids at the base of the tree hierarchy, and hence have no parents. We also impose two density-based criteria on our void catalogue. The first is a threshold cut within ZOBOV itself where voids only include as members Voronoi cells with density less than 0.2 the mean particle density. We apply the second density criterion as a post-processing step: we only include voids with mean central densities below 0.2 the mean particle density. We measure this central density within a sphere with radius  $R = 1/4R_{\text{eff}}$ , where

$$R_{\text{eff}} \equiv \left( \frac{3}{4\pi} V \right)^{1/3}. \quad (3)$$

In the expression above,  $V$  is the total volume of the void. We also ignore voids with  $R_{\text{eff}}$  below the mean particle spacing of the tracer population.

Additionally, for the analysis below, we need to define a centre for the void. For our work, we take the barycentre, or volume-weighted centre of all the Voronoi cells in the void:

$$\mathbf{X}_v = \frac{1}{\sum_i V_i} \sum_i \mathbf{x}_i V_i, \quad (4)$$

where  $\mathbf{x}_i$  and  $V_i$  are the positions and Voronoi volumes of each tracer  $i$ , respectively.

Table 1 summarizes the samples used in this work, their minimum effective void radius, and the number of voids identified in the simulation volume.

## 3 VOID HIERARCHIES

As discussed in Lavaux & Wandelt (2012) and Aragon-Calvo & Szalay (2013), watershed void finders naturally group voids into a nested hierarchy of parents and children. We may use this hierarchy

**Table 1.** Summary of sample void populations.

Data set type	Sample name	$R_{\text{eff, min}} (h^{-1} \text{ Mpc})$	$N_{\text{voids}}$
DM	DM Full	5	42 948
DM	DM Dense	7	21 865
Halo	Halo Dense	7	11 419
HOD	HOD Dense	7	9503
DM	DM Sparse	14	2611
Halo	Halo Sparse	14	2073
HOD	HOD Sparse	14	1422

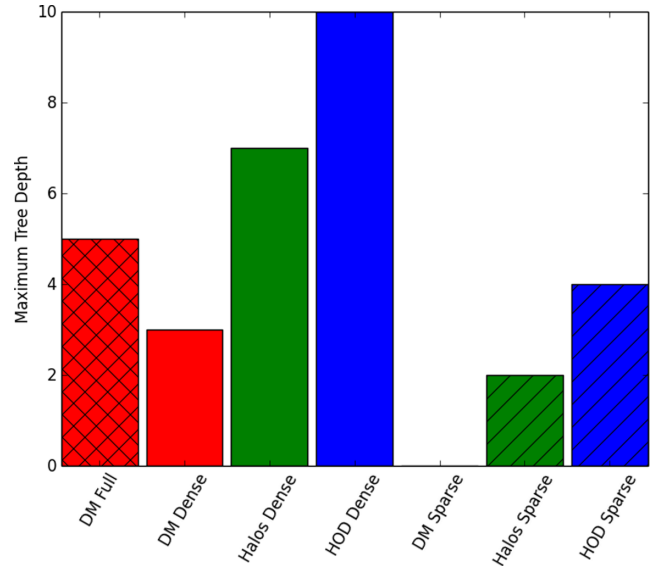


**Figure 1.** Maximum tree depth in the void hierarchy for each sample. In addition to the axis labels, bars are coloured by sample type: red for dark matter, green for haloes, and blue for galaxies. Double-hatched bars represent *Full* resolution samples, *Dense* samples are shown with no hatching, and *Sparse* samples are shown with single-line hatches. Subsampling of the dark matter destroys the void hierarchy, while using biased tracers such as galaxies and haloes reinforces the hierarchy.

to understand the effects of subsampling and biasing before we turn to the observational consequences. We define the void tree such that each void has only a single parent (or no parents at all), and can potentially have many children. One void is considered a parent of another if it shares all zones of the child plus at least one more. Parents can then become children of even larger voids. Without any density thresholds, there will be a single void that encompasses the entire simulation volume and that serves as the root void for the entire population. However, since we do apply a density threshold, we have multiple root voids.

Fig. 1 shows the maximum tree depth for each sample. The maximum tree depth is the length from root to tip of the tallest tree in the hierarchy, and gives a measure of the amount of substructure in the most complex void in the sample. For comparison, the hierarchical tree depth of voids in a Poisson distribution of particles is identically zero. This follows from the high improbability of producing large voids in a Poisson distribution, and from the fact that substructures arise naturally from hierarchical formation.

We immediately notice the effects of lowering the sampling density: we completely erase any substructure information in the *DM Sparse* sample. In contrast, even though the halo and galaxy populations have overall lower mean density, since they are *biased* tracers, they naturally more strongly trace the substructure. Unsurprisingly, lower density galaxy (and halo) populations have less substructure than their high-density counterparts. Additionally, galaxy populations, which are based on their respective halo catalogues but have more tracers, display more substructure.

We can understand these results by looking at the density contrasts of the void populations. We define the density contrast of a void as the ratio between the mean density of particles along the wall to the density of the least-dense (or ‘core’) particle. In ZOBOV, particles along the void wall are easy to identify: they are adjacent to at least one non-void particle. Fig. 2 shows the density contrast

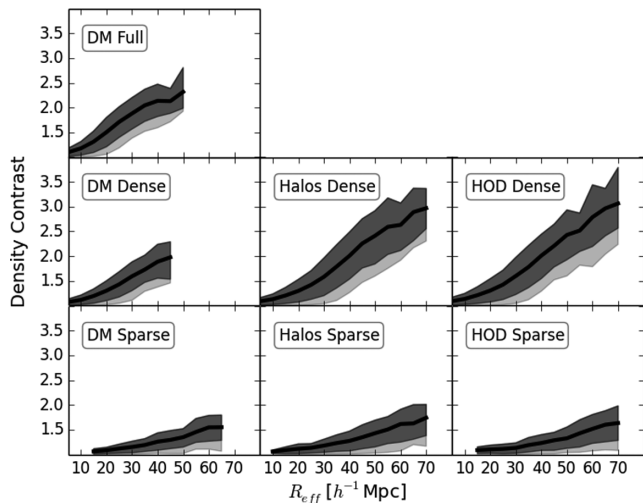


**Figure 2.** Void density contrast (ratio between the mean density of particles along the wall to the density of the least-dense particle) versus void effective radius. Solid lines are the mean of the density contrast in thin bins of  $R_{\text{eff}}$  and dark (light) grey bands are  $1\sigma$  ( $2\sigma$ ) ranges of the distribution in those bins. All samples show a trend of increasing density contrast with void size. Haloes and galaxies produce very high-density contrasts since many tracers are placed along the filaments and walls.

versus void effective radius for each sample. While there is considerable scatter in the relations, the density contrasts of our highest density sample, *DM Full*, clearly show steep dependence on void radius. We might naively expect the opposite trend, because smaller voids tend to have higher walls due to the *void-in-cloud* process (Sheth & van de Weygaert 2004). However, even though the larger voids contain significant substructure, they tend to have very deep underdense subregions inside them, thus producing larger maximum contrasts. As we lower the sampling density, we find larger voids (which we will discuss in more detail below) but also much shallower voids: the maximum density contrast in the *DM Sparse* sample is only  $\sim 1/3$  the maximum contrast in the *DM Full* sample. This behaviour is entirely expected: as we remove particles, we ‘thin out’ the walls that define the void boundaries, and thus reduce the overall density at the edges.

However, both the halo and HOD samples, even though they contain fewer tracers than the high-resolution dark matter cases, have comparable – and even higher – density contrasts than the low-resolution dark matter samples. We expect this because of biasing: we generally make the walls thinner by switching to haloes and galaxies, leading to larger voids, but the walls that survive are more densely concentrated with tracers, leading to high-density contrasts. The relationship between density contrast and radius is nearly identical between voids in galaxies and haloes, since they are both already biased tracers.

We may also consider the position of the void in the tree hierarchy. All root voids have a broad range of density contrasts, since these include isolated small voids with low-density contrasts and large voids that serve as parents of subvoids. On the other hand, for all samples, the most deeply nested voids exclusively have low-density contrasts. Thus, we clearly see that as we lower the sampling density, we puncture lower density walls, allowing the watershed algorithm to join adjacent basins, and more preferentially erase smaller, deeply nested voids. Voids that happen to have high-density walls tend to survive. The HOD and halo samples are able to recover substructure by selectively placing tracers along the walls and filaments that separate voids.

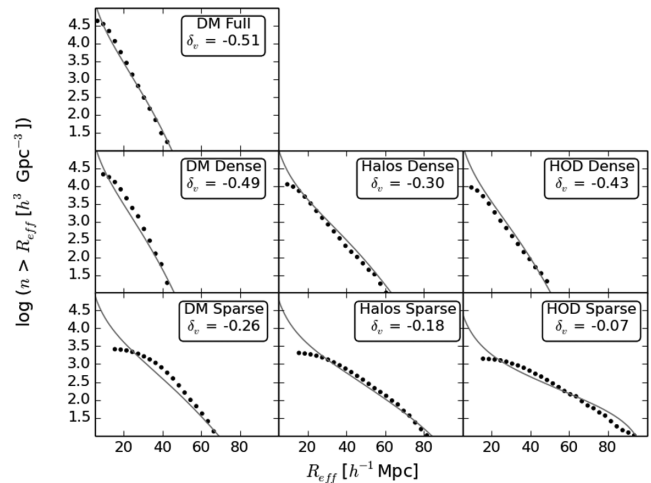


**Figure 3.** Cumulative void number function. The dotted lines are measured number functions in each indicated sample, and the thin grey lines are theoretical predictions of the *SvdW* function with the  $\delta_v$  parameter adjusted to the indicated value. The best-fitting parameter value is shown in each subplot.

## 4 VOID STATISTICS

### 4.1 Number functions

Perhaps the most fundamental void statistic is the void number function: the number of voids of a given size per unit volume. Since the growth of voids is intimately tied to the growth of structure, which is itself controlled by the nature of dark energy and the amount of dark matter in the universe, the void number function is sensitive to cosmological parameters (e.g. Jennings et al. 2013). Since different cosmologies affect the number function in different ways (e.g. by suppressing the formation of larger voids and thereby tilting the distribution), we must disentangle the effects of sparsity and biasing, which can modify the number function in similar ways.

Fig. 3 shows our cumulative void number function for each sample. As previous authors (Colberg et al. 2005; Jennings et al. 2013; Watson et al. 2014) have noted, voids in lower density samples tend to be larger, and there tend to be fewer small voids. This is due to two causes. Firstly, the walls and filaments are thinner in low-density samples, leading to the same population of voids as in high-density samples, but the individual voids are just larger. Secondly, if a lower density wall separating two voids loses too many particles due to subsampling, the watershed method will merge the two basins without first identifying them as separate voids. In Sutter et al. (2014), we examine the relative importance of these two effects for different galaxy sampling densities. For this work, we ignore the underlying causes and focus on the observational consequences.

We see that the void number functions from halo catalogues closely follow that of the mock galaxy catalogues, as we expected from the discussion in the previous section. The difference between the *DM Sparse* and *HOD Sparse* is due to the interaction between biasing and our central density cut. At fixed tracer density, a more biased tracer will lead to a sharper density contrast for a given size of void. Biasing concentrates tracers along the walls enhancing the density contrast, see Fig. 2 and the associated discussion. Therefore, large voids found in biased tracers will tend to survive a central density cut in spite of the voids being partially filled with dark matter. The corresponding shallow underdensities in the dark matter sample have more substructure, and will therefore not survive the density

cut. In the high-resolution cases, the substructure remains even in the biased tracers, rendering this effect much less pronounced.

To provide theoretical number functions, we turn to the analysis of Sheth & van de Weygaert (2004, hereafter *SVdW*), who employ the excursion-set formalism to develop a void number function of the form

$$n(M) = \frac{\bar{\rho}}{M^2} \nu f(\nu) \frac{d \ln \nu}{d \ln M}, \quad (5)$$

where  $\bar{\rho}$  is the background matter density,  $M$  the void mass,  $\nu = \delta_v^2 / \sigma^2(M)$  with  $\delta_v$  being the critical underdensity for void formation and  $\sigma^2(M)$  the variance of the density field on a scale  $R \simeq (3M/4\pi\bar{\rho})^{1/3}$ , and

$$\nu f(\nu) = \sqrt{\frac{\nu}{2\pi}} \exp\left(-\frac{\nu}{2}\right) \exp\left(-\frac{|\delta_v| \mathcal{D}^2}{\delta_c} \frac{1}{4\nu} - 2\frac{\mathcal{D}^4}{\nu^2}\right). \quad (6)$$

Here,  $\mathcal{D} \equiv |\delta_v| / (\delta_c + |\delta_v|)$  is the so-called *void-and-cloud* parameter, which determines the relative importance of halo and void formation. The value for the critical overdensity of collapse  $\delta_c \simeq 1.686$  is tightly constrained by the spherical collapse model, but Furlanetto & Piran (2006) pointed out that the value of  $\delta_v$  must be adjusted to account for the sampling density of the tracers used to identify voids.

While there have been attempts to improve this basic relation (Paranjape et al. 2012; Achitouv et al. 2013; Jennings et al. 2013), they still require parameter adjustments to translate between void populations in dark matter and galaxies. Until the development of a robust dynamics-based prediction for the void number function that automatically accounts for sparsity and biasing, we should take these models as a basis for phenomenologically fitting to void populations in dark matter and mock galaxy catalogues.

In that spirit, we employ the fixed radial rescaling of 1.7 described in Jennings et al. (2013), and adjust the  $\delta_v$  parameter to attempt to fit our measured void number functions. Attempts to rescale the radii beyond the fixed value of 1.7 did not produce better fits. We show these best-fitting values in Fig. 3. While the simple functional form of equation (5) matches the rough order of magnitude and approximate shape for each sample, it misses the detailed shape, and thus we do not evaluate a goodness of fit.

Although we are unable to match the detailed shape of the number function with the *SVdW* functions, we do match the gross properties and overall number counts with surprising ease: a single parameter adjustment allows us to approximate the number functions in both high- and low-resolution samples of all tracer types, although it is more difficult to account for the effect of biasing on large voids. We see that the void number function is more dependent on the density of tracers rather than the type of tracers, and that we can divide our samples into low- and high-resolution groups.

The values of  $\delta_v$  shown in Fig. 3 stand in contrast to the expected  $\delta_v = -2.8$  based on shell-crossing criteria for spherical underdensities (*SVdW*; Biswas et al. 2010). Two factors contribute to this difference: our void finder discovers the full non-spherical shape of the underdensity, so the spherical approximation breaks down, and the assumption of complete shell-crossing across the entire void surface is too restrictive in general (Falck, Neyrinck & Szalay 2012; Neyrinck, Falck & Szalay 2013).

## 4.2 Ellipticity distributions

There has been considerable interest recently in the dependence of void shapes on the nature of dark energy (e.g. Lee & Park 2006; Park & Lee 2007; Biswas et al. 2010; Bos et al. 2012). The shape

distribution of voids is the inverse of the growth of structure: as matter collapses to form galaxies, groups, and clusters, the shapes of the evacuated regions will necessarily change. Since measurements of voids are largely unaffected by systematics due to baryonic physics, the redshift evolution of the void shape distribution potentially serves as a powerful tracer of dark energy. In addition, the mean stretch of voids along the line of sight may be used for an application of the Alcock–Paczynski test (Alcock & Paczynski 1979; Ryden 1995; Lavaux & Wandelt 2012; Sutter et al. 2012b).

We will simplify the discussion of void shapes by focusing on the ellipticity. To compute the ellipticity, for a given set of tracers within a void we first construct the inertia tensor:

$$M_{xx} = \sum_{i=1}^{N_p} (y_i^2 + z_i^2)$$

$$M_{xy} = - \sum_{i=1}^{N_p} x_i y_i, \quad (7)$$

where  $N_p$  is the number of particles in the void, and  $x_i$ ,  $y_i$ , and  $z_i$  are coordinates of the particle  $i$  relative to the void barycentre. The other components of the tensor are obtained by cyclic permutations. Given the inertia tensor, we compute the eigenvalues and form the ellipticity:

$$\epsilon = 1 - \left(\frac{J_1}{J_3}\right)^{1/4}, \quad (8)$$

where  $J_1$  and  $J_3$  are the smallest and largest eigenvalues, respectively.

Fig. 4 shows the ellipticity distribution for each sample. We contrasted these ellipticities to the ellipticities of voids found in a random Poisson distribution of particles with density  $10^{-2}$  tracers per cubic  $h^{-1}$  Mpc. Voids in all samples are more elliptical and have broader distributions than voids in random particles. For each type of tracer, the amount of ellipticity of the voids correlates with the density of the underlying tracer population: lower density tracers produce more spherical voids. This is mainly due to the loss of the smallest voids, which tend to have higher ellipticities (Sutter et al.

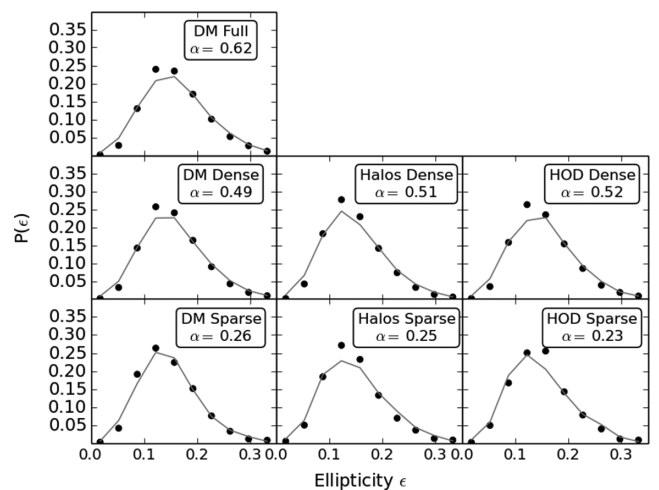


**Figure 4.** Measured ellipticity distributions (points) for each sample and best-fitting theoretical distributions (thin grey lines). To produce the theoretical distributions we use DIVA with the rescaling parameter shown in each subplot. This rescaling parameter  $\alpha$  (equation 9) sets the scaling from Eulerian to Lagrangian scales.

2013) than medium-scale voids, which survive at lower sampling density.

Comparing samples at fixed density against each other, we see that haloes produce more spherical voids, while galaxies recover similar ellipticities as the original dark matter samples, although for the *Sparse* samples the ellipticities are largely indistinguishable. The halo populations produce more spherical voids because of the lack of tracers for the smallest void populations. However, the presence of satellites in the HOD galaxy populations generally adds more tracers along the void boundaries giving better shape measurements, and hence higher ellipticities. This same phenomenon – that of increased hierarchical structure in the HOD population – gives rise to the more substantial tree structure in Fig. 1. Thus, results such as Bos et al. (2012), which use voids in halo populations to assess the power of void ellipticities in galaxy surveys to constrain exotic dark energy models, may be too pessimistic.

To compare to theoretical expectations, we use the Lagrangian model of Lavaux & Wandelt (2010) developed in the context of DIVA (Dynamical Void Analysis), a Lagrangian void finder and characterizer. DIVA is based on the capability to compute the Lagrangian comoving coordinates of any particles or galaxies from solely its Eulerian position. This capability is provided by the Monge–Ampère–Kantorovitch (MAK) reconstruction (Brenier et al. 2003; Lavaux et al. 2008). From the mass tracer distribution at a given redshift  $z$ , MAK finds the proper change of coordinates to map the position of the tracers at high redshift such that the density becomes totally homogeneous. Through this transformation, we may model very accurately the distribution and the evolution of ellipticity with redshift.

Lavaux & Wandelt (2010) showed that to first order the inertial tensor estimate of the ellipticity and its counterpart estimated from dynamics are equivalent, though with large scatter. We compare the analytical model of the evolution of the ellipticity to our measured ones obtained from the inertial tensor method, neglecting the impact of the scatter. To do so, we need to select a proper smoothing scale for the Lagrangian calculation in DIVA, and the link between this smoothing scale and the Eulerian radius that we measure in simulations and data is not clear. For simplicity, we will assume a simple scaling in which for a void of given radius  $R_{\text{eff}}$  we choose a smoothing scale

$$R_0 = \alpha R_{\text{eff}}, \quad (9)$$

where  $\alpha$  is a free parameter. As discussed in Lavaux & Wandelt (2010), we may identify the Eulerian ellipticity  $\epsilon$  with the Lagrangian eigenvalues  $\lambda_i$  of the gravitational shear tensor via

$$\epsilon \cong 1 - \left( \frac{1 + \lambda_1}{1 + \lambda_3} \right)^{1/2}, \quad (10)$$

where  $\lambda_1$  is the smallest eigenvalue and  $\lambda_3$  is the largest. For each individual void, we choose the smoothing scale with equation (9) and compute the distribution of ellipticities (equation 10). We then draw an ellipticity from a Gaussian distribution with the same mean and variance. This is simply for numerical convenience but approximates well the actual distribution. We take this randomly chosen ellipticity as the predicted ellipticity of that void. Finally, we build a distribution of the predicted ellipticities for comparison to the distribution of ellipticities as measured in our simulation with equation (8).

Fig. 4 shows the measured ellipticity distributions for each sample as well as the theoretical distributions with best-fitting values of  $\alpha$ . We found that for higher resolution samples (*DM Full* and *HOD Dense*), a choice of  $\alpha = 0.5$ – $0.6$  produced theoretical distributions

in excellent agreement with the measured distributions: not only do we match the mean ellipticities, but we also broadly recover the shapes of the distributions. For sparse samples, a value of  $\alpha \sim 0.25$  was more appropriate. This change in the parameter  $\alpha$  to accommodate low-resolution samples is analogous to the need to change  $\delta_v$  for number functions. In this case, lower values of  $\alpha$  indicate that the dynamical cores of voids in the *Sparse* samples are smaller than in the higher resolution samples, in line with the preceding number function analysis.

### 4.3 Radial density profiles

The radial density profiles of voids are exceptionally sensitive to modified gravity and fifth forces, since the absence of matter allows exotic forces to remain unscreened (Clampitt et al. 2013; Spolyar et al. 2013). However, since the choice of mass tracer can also affect density profiles (Benson et al. 2003; Colberg et al. 2005; Padilla et al. 2005), we must first understand the impacts of sparsity and biasing before using voids as probes of fundamental physics. If we can provide a translation from theoretical predictions in dark matter to observational radial profiles, we can forecast if modifications due to exotic forces will persist when using galaxies to define voids.

Fig. 5 shows one-dimensional radial profiles for all samples in a few selected radius ranges. To compute the profiles, we take all voids in a sample of a given size range (e.g.  $30$ – $35 h^{-1}$  Mpc), align all their barycentres, and measure the density in thin spherical shells. We normalize each density profile to the mean number density of the sample and show all profiles as a function of relative radius,  $R/R_v$ , where  $R_v$  is the median void size in the stack.

Many authors have discussed and presented measured radial density profiles in data and simulations, and there appears to be a generally universal shape to the profile: a central underdense floor, a steep wall, a slightly overdense compensation, and a declining density that asymptotes to the mean density (e.g. Benson et al. 2003; Padilla et al. 2005; Ceccarelli et al. 2006; Lavaux & Wandelt 2012; Sutter et al. 2012a). The *internal* density profiles of voids are nearly identical across all samples, with lower density samples producing slightly steeper slopes, lending further evidence for the existence of this universal void profile and that sparsity and galaxy bias do not impact this profile much.

However, the *external* void profile shows significant differences among the samples. The height of the compensation bump depends on the surrounding medium and is generally dependent on void size: small voids are typically found in large overdense regions (the *void-in-cloud* process) and large voids are typically found in underdense regions (the *void-in-void* process). This separation of void types was first discussed in SVdW and measured in SDSS voids by Ceccarelli et al. (2013).

For a stack of voids of a given size range, low-density samples of all types appear more overcompensated, and high-density samples appear more undercompensated with shallower slopes and lower compensation regions. Comparing samples at a given density, the slopes of the profiles are very similar but with different compensation heights, due to the biasing of the galaxies and haloes relative to the dark matter. This may seem counterintuitive given our measurements of the density contrasts in Fig. 2. However, that measurement was a comparison of the density of the core particle (not a spherically averaged volume as in these plots) to the density on the wall of the void, which is just inside the compensation region.

As with the number functions, we see that haloes offer a good proxy for the galaxy population. Interestingly, *all* halo and galaxy populations, regardless of sampling density, produce very

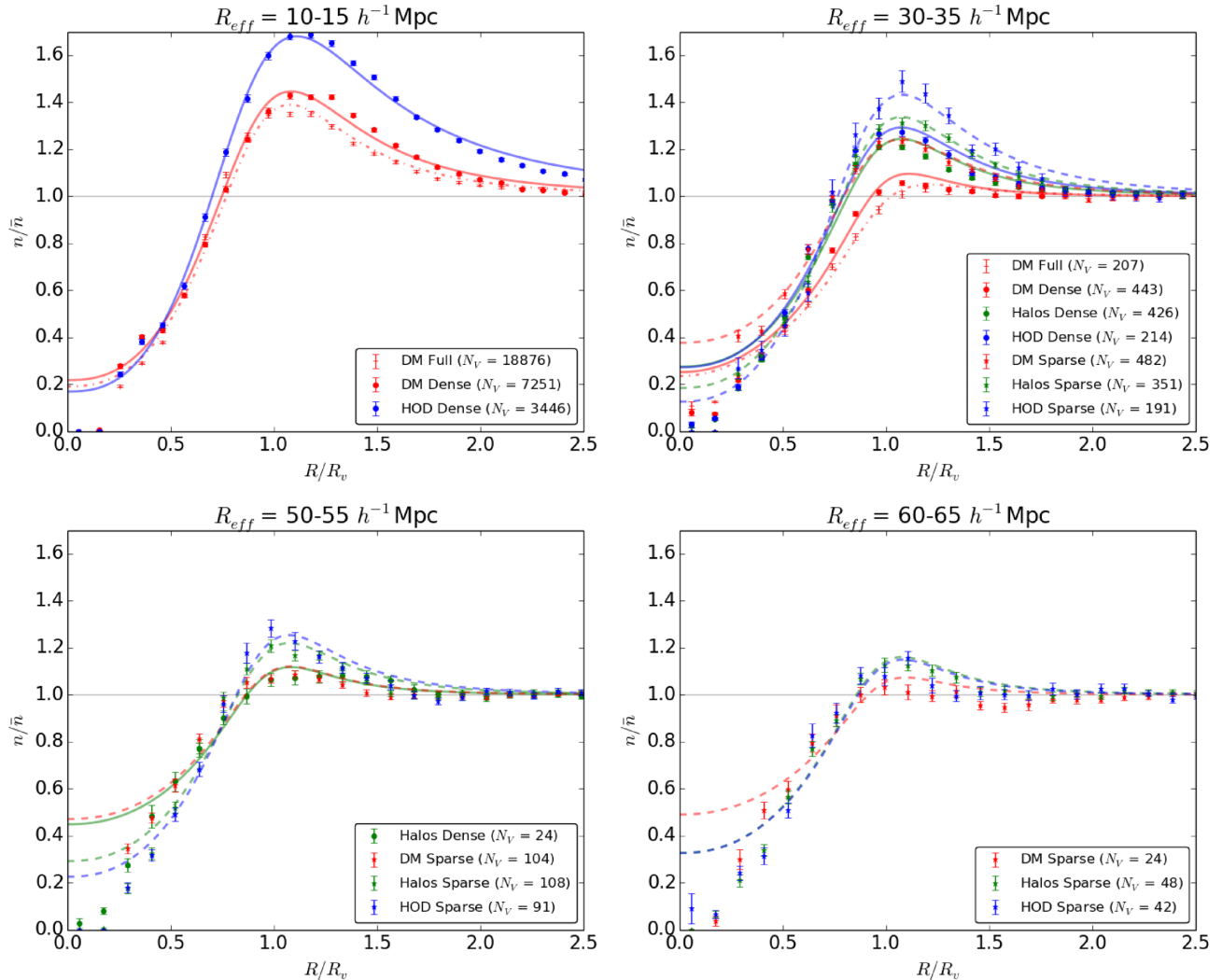


**Figure 5.** One-dimensional radial density profiles of stacked voids (points with error bars) and best-fitting curves (thin lines) using the profile discussed in equation (11). For the fit, we ignore the first three bins, since these are artificially influenced by numerical effects in the simulation and the application of the central density cut. Each profile is normalized to the mean number density  $\bar{n}$  of that sample and  $R_v$  corresponds to the median void size in the stack. Solid coloured lines are from high-density samples, and dotted coloured lines are from low-density samples. Each tracer type is given a unique colour and symbol as indicated in the legend. The best-fitting values are plotted in Fig. 6.

similar radial profiles. This is likely due to the fact that the radial profile is more sensitive to the biasing of the tracers than to the density. Indeed, in this context, we can understand biasing as just another form of subsampling: biased but high-density populations (e.g. *HOD Dense*) act very similarly to unbiased but low-density populations (e.g. *DM Sparse*). This is in contrast with the effect on number functions: there, sparsity was more important than biasing. However, the number functions probe the interior contents of voids, and this discussion has focused mainly on the compensation, which is in the *surrounding* medium.

There is very little theoretical development into *predictions* for the shapes of profiles. Given the lack of theoretical motivation, authors generally attempt fits to the radial density profile using an empirical formula that attempts to reproduce the profile shapes. We use the recent profile described in Hamaus, Sutter & Wandelt (2014b), which includes a functional form spanning both the interior void slope and the compensation region:

$$\frac{n}{\bar{n}}(r) = \delta_c \frac{1 - (r/r_s)^{\alpha(r_s)}}{1 + (r/R_v)^{\beta(r_s)}} + 1, \quad (11)$$

where Hamaus et al. (2014b) found that

$$\alpha(r_s) \simeq -2.0(r_s/R_v) + 4.0 \quad (12)$$

$$\beta(r_s) \simeq \begin{cases} 17.5(r_s/R_v) - 6.5 & \text{if } r_s/R_v < 0.91 \\ -9.8(r_s/R_v) + 18.4 & \text{if } r_s/R_v > 0.91. \end{cases} \quad (13)$$

There are two free parameters to this model:  $r_s$ , the radius at which the profile reached mean density, and  $\delta_c$ , the underdensity in the central core. Fig. 6 shows the best-fitting values of  $\delta_c$  and  $r_s$  for all void stacks in all samples. This two-parameter model describes nearly all voids very well, although we see that it has difficulty reproducing the exact height of the compensation bump for the very largest voids. This is due to the fact that equation (13) is tuned to voids in high-resolution dark matter, and not necessarily appropriate for these cases. Despite this, however, the fits agree remarkably well.

We can understand these differences in terms of the void size at which the void bias changes sign (Hamaus et al. 2014a): the compensation scale. This change in the bias represents a switch from generally overcompensated to generally undercompensated voids.

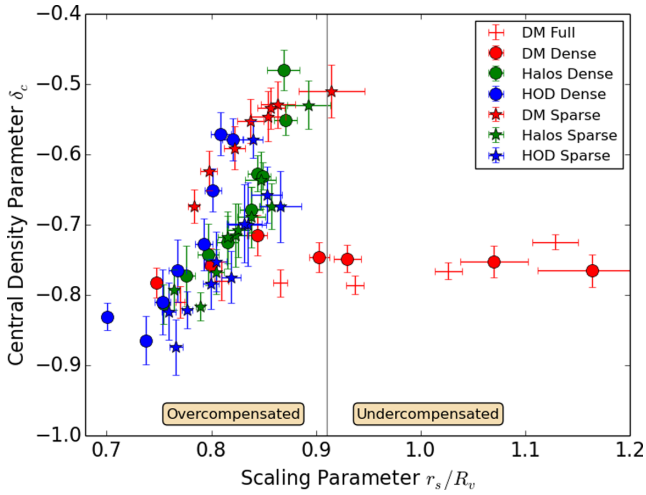


**Figure 6.** Best-fitting values and  $1\sigma$  uncertainties for all void stacks in all samples. Tracer types are distinguished by colours and densities by symbol, as noted in the legend. The thin grey line depicts the compensation scale.

Voids in higher density tracers have a smaller compensation scale than voids in low-density tracers. Thus, if we choose a stack of voids with radii well below this compensation scale for all tracers, for example  $10\text{--}15 h^{-1}$  Mpc, then the profiles will look very similar. Similarly, if we stack very large voids, we only see undercompensated voids and again the profiles are similar. For intermediate scales, high-density tracers such as *DM Full* will have switched from over- to undercompensation, while low-density tracers will remain overcompensated. This manifests in the different slopes and compensation heights in the profiles from  $\sim 20$  to  $\sim 50 h^{-1}$  Mpc. Note that this is a continuous progression from over- to undercompensation, so generally as we increase the stack size we see gradually reduced compensations.

Thus, we can in principle rescale any void from any tracer population on to any other void from any other tracer population, and Fig. 7 demonstrates such rescaling. In this figure, we plot each fitting parameter separately as a function of void size for each sample. By choosing a single fiducial parameter value, we rescale all void radii in a sample with only a single scale factor. In other words, we can pick any parameter–radius relationship from any sample and shift all of the other relations on top of it by simply rescaling

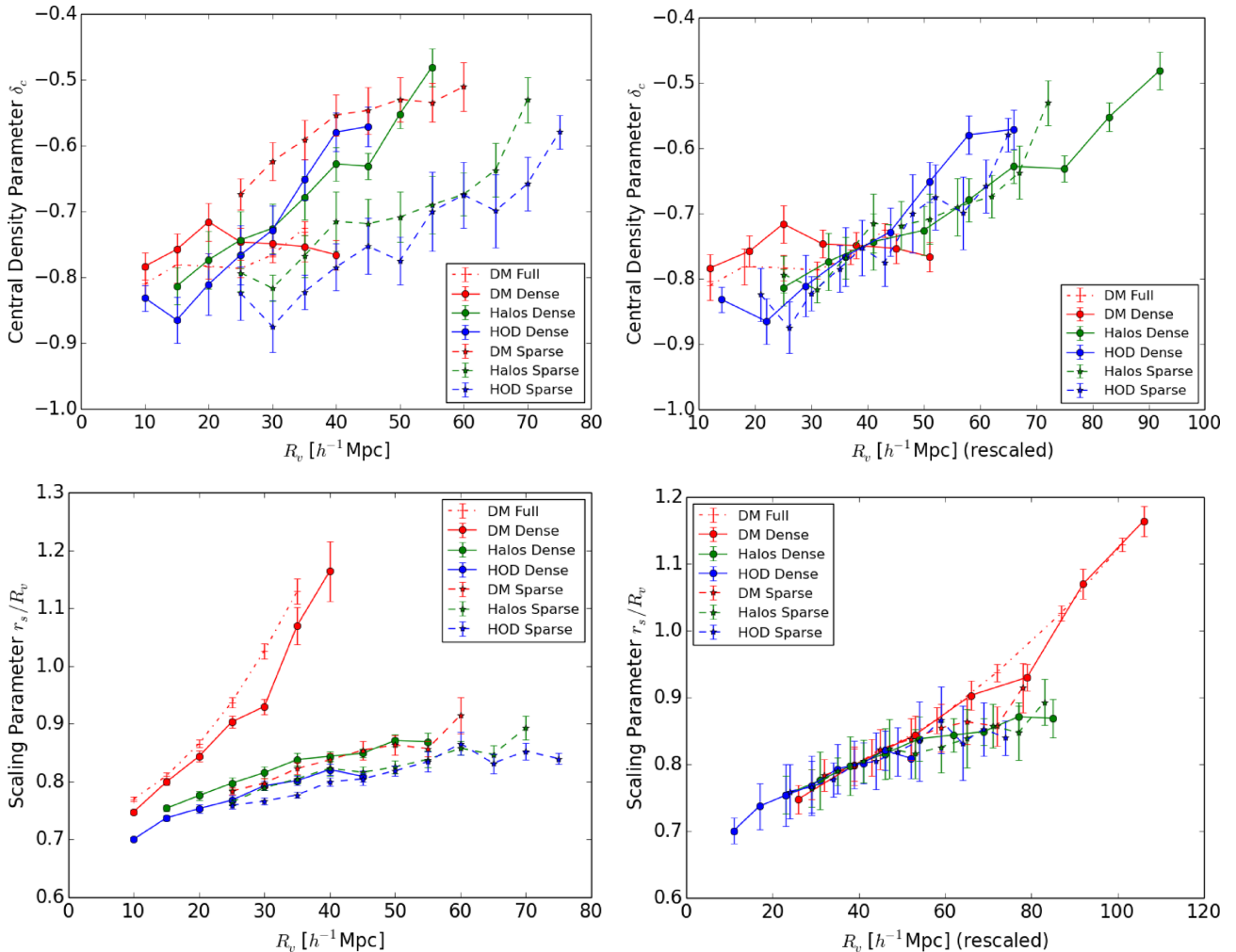


**Figure 7.** Universal rescaling of voids. We show the fitting parameter  $\delta_c$  versus void radius  $R_v$  in the top row, and the bottom row shows  $r_s$  versus void radius  $R_v$  for each sample. The left-hand column is the non-rescaled fitting parameters. On the right, we pick a fiducial point in the plane and rescale all voids in a given sample by a single value so that the parameter–size curve passes through that point. After rescaling, the curves cluster around a universal relationship between void size and the fitting parameters that is independent of tracer density and bias.

each of their void radii by a single number. When this is performed for each sample, the curves cluster around a universal relationship between void size and the fitting parameters that is independent of sample density and bias.

## 5 CONCLUSIONS

By using direct subsampling, halo finding, and HOD modelling on a single high-resolution, large-volume  $N$ -body simulation, we have carefully investigated the impacts of tracer density and biasing on void statistics. We have used the void tree hierarchy to understand the impacts on number functions, ellipticities, and density profiles. We find that sampling density is much more important for measured void properties than galaxy bias. As we lower the tracer density, voids become larger, small voids disappear, they become more spherical, and their profiles become slightly steeper. The biasing due to galaxy tracers recovers some of the loss of information due to low densities: the tree hierarchy is restored and void walls become steeper, leading to higher ellipticities. This kind of hierarchical tree analysis can be directly applied to voids in observations, since it is a natural feature of the watershed algorithm and already implemented in our approach described in Sutter et al. (2012a). However, the limited survey volumes available in the SDSS prevent a detailed examination at this time.

We have used theoretical and empirical formulas to model the statistical void properties as a function of tracer type and density:

*Number functions.* The SVdW number function approximates well the behaviour of measured number functions with simple adjustments to the ‘void parameter’  $\delta_v$ , although further work is needed to model specific shapes. These adjustments make sense since the  $\delta_v$  parameter relates the size of a void to the central underdensity in the dark matter. Since number functions of voids in low-density samples are best fitted by lower values of  $\delta_v$ , this tells us that the voids discovered in low-density surveys, while still underdense, represent very shallow, wide density perturbations, as seen in the HOD modelling analysis of Sutter et al. (2014) and the ab initio simulations of Ricciardelli, Quilis & Varela (2014).

*Ellipticity distributions.* Here, semi-analytic calculations are able to describe with very high fidelity the statistics of void ellipticities. One can take a mock void population (either produced from simulations or from a theoretical distribution), rescale appropriately, and estimate the resulting ellipticity distribution with methods such as DIVA. The rescaling parameter  $\alpha$  must be adjusted to account for the sparsity of the survey:  $\alpha \sim 0.5$  is appropriate for high-resolution surveys, while  $\alpha \sim 0.25$  is necessary for low-resolution surveys. Once this single choice of parameter is made, there is remarkably good agreement in both the mean and the shape of the distributions. This change in the required value of  $\alpha$  is consistent with the change in  $\delta_v$ , since  $\alpha$  connects the Eulerian size of a voids to its Lagrangian size, and sparser samples will map out larger Eulerian volumes around the same core underdensity.

*Radial profiles.* While there is limited theoretical motivation for any particular void profile at all scales (although, as discussed in Pápai, Szapudi & Granett 2011, for large enough scales the BBKS formalism provides an expected profile), the function of Hamaus et al. (2014b) describes all voids in all samples to a remarkable degree of accuracy. Using this fit, we have shown that voids obey a universal and self-similar relationship between central underdensity, scaling radius, and size. Thus, voids in one sample or survey can be immediately rescaled to match voids in another sample or survey, even from high-resolution  $N$ -body simulations to a sparse galaxy survey.

We have also judged the ability of haloes to approximate the galaxy distribution, a common approach, since HOD and SAM are subtle and computationally expensive. We found that for number functions and radial profiles, this is a good approximation, but *only when an appropriate minimum mass threshold is chosen*, specifically by matching the abundances of central galaxies. This is similar to the conclusions of Padilla et al. (2005). Simulations have a variety of volume and resolutions, and the minimum halo mass in a given simulation may not correspond to any particular survey. Care must be taken to make predictions for specific surveys. Also, we found that voids in halo distributions are more spherical than in galaxy distributions: for ellipticity predictions, either a constant shift to account for galaxies or an approach like DIVA must be used.

This work is only a first step: we have looked at sparsity and biasing, but ignored redshift space distortions and effects of survey masks. In the case of radial profiles, we may use techniques such as those described in Pisani et al. (2013) to translate from redshift to real space and make contact with our results. The early work of Ryden & Melott (1996) has looked at void shapes in real- versus redshift-space, but a more comprehensive study is needed. Our companion work (Sutter et al. 2013) includes a preliminary analysis of the impact of survey masks.

We have made all populations (dark matter, haloes, and mock galaxies) used in this work as well as the resulting void information publicly available alongside our catalogue of voids in the SDSS DR7 and DR9 at <http://www.cosmicvoids.net>. The formatting of the catalogue follows that described in the appendix of Sutter et al. (2012a). The catalogue contains a README with more detailed information.

While our recommendations obviously depend on specific survey details, we have provided broad guidelines for judging the feasibility of a particular void statistic to inform us about cosmology. By quantifying the effects of sparsity and biasing, we can translate between results in theory, high-resolution dark matter, and current and future galaxy surveys. Also, our discovery of a simple rescaling of void density profiles suggests that we may study voids in dark matter and trivially make predictions for voids in galaxy surveys, regardless of sampling density and bias. This allows future work to disentangle these effects from cosmological signals, opening the way for more effective and straightforward void cosmology predictions.

## ACKNOWLEDGEMENTS

PMS, NH, and BDW acknowledge support from NSF Grant NSF AST 09-08693 ARRA. BDW also acknowledges funding from an ANR Chaire d’Excellence (ANR-10-CEXC-004-01), the UPMC Chaire Internationale in Theoretical Cosmology, and NSF Grants AST-0908 902 and AST-0708849. GL acknowledges support from CITA National Fellowship and financial support from the Government of Canada Post-Doctoral Research Fellowship. Research at Perimeter Institute is supported by the Government of Canada through Industry Canada and by the Province of Ontario through the Ministry of Research and Innovation. DW acknowledges support from NSF Grant AST-1009505. This work made in the ILP LABEX (under reference ANR-10-LABX-63) was supported by French state funds managed by the ANR within the Investissements d’Avenir programme under reference ANR-11-IDEX-0004-02.

## REFERENCES

Achitouv I., Neyrinck M., Paranjape A., 2013, preprint (arXiv:1309.3799)  
Alcock C., Paczynski B., 1979, *Nature*, 281, 358

- Aragon-Calvo M. A., Szalay A. S., 2013, *MNRAS*, 428, 3409
- Beck A. M., Hanasz M., Lesch H., Remus R.-S., Staszyszyn F. A., 2013, *MNRAS*, 429, L60
- Behroozi P. S., Wechsler R. H., Wu H., 2013, *ApJ*, 762, 109
- Benson A. J., Hoyle F., Torres F., Vogeley M. S., 2003, *MNRAS*, 340, 160
- Biswas R., Alizadeh E., Wandelt B., 2010, *Phys. Rev. D*, 82, 023002
- Blas D., Lesgourgues J., Tram T., 2011, *J. Cosmol. Astropart. Phys.*, 11, 07
- Bos E. G. P., van de Weygaert R., Dolag K., Pettorino V., 2012, *MNRAS*, 426, 440
- Brenier Y., Frisch U., Hénon M., Loeper G., Matarrese S., Mohayaee R., Sobolevskii A., 2003, *MNRAS*, 346, 501
- Ceccarelli L., Padilla N. D., Valotto C., Lambas D. G., 2006, *MNRAS*, 373, 1440
- Ceccarelli L., Herrera-Camus R., Lambas D. G., Galaz G., Padilla N. D., 2012, *MNRAS*, 426, L6
- Ceccarelli L., Paz D., Lares M., Padilla N., García Lambas D., 2013, *MNRAS*, 434, 1435
- Clampitt J., Cai Y.-C., Li B., 2013, *MNRAS*, 431, 749
- Colberg J. M., Sheth R. K., Diaferio A., Gao L., Yoshida N., 2005, *MNRAS*, 360, 216
- Croce M., Pueblas S., Scoccimarro R., 2006, *MNRAS*, 373, 369
- Dawson K. S. et al., 2013, *AJ*, 145, 10
- De Lucia G., 2009, in Giobbi G., Tornambe A., Raimondo G., Limongi M., Antonelli L. A., Menci N., Brocato E., eds, *AIP Conf. Proc. Vol. 1111, Probing Stellar Populations Out to the Distant Universe: CEFALU 2008*. Am. Inst. Phys., New York, p. 3
- Dehnen W., 2001, *MNRAS*, 324, 273
- Dubinski J., da Costa L. N., Goldwirth D. S., Lecar M., Piran T., 1993, *ApJ*, 410, 458
- Falck B. L., Neyrinck M. C., Szalay A. S., 2012, *ApJ*, 754, 126
- Ferreras I., Pasquali A., eds, 2011, *Environment and the Formation of Galaxies: 30 Years Later*. Springer-Verlag, Berlin
- Fillmore J. A., Goldreich P., 1984, *ApJ*, 281, 9
- Furlanetto S. R., Piran T., 2006, *MNRAS*, 366, 467
- Gottlobber S., Lokas E. L., Klypin A., Hoffman Y., 2003, *MNRAS*, 344, 715
- Hamaus N., Wandelt B. D., Sutter P. M., Lavaux G., Warren M. S., 2014a, *Phys. Rev. Lett.*, 112, 041304
- Hamaus N., Sutter P. M., Wandelt B. D., 2014b, preprint ([arXiv:1403.5499](https://arxiv.org/abs/1403.5499))
- Ilic S., Langer M., Douspis M., 2013, *A&A*, 556, A51
- Jennings E., Li Y., Hu W., 2013, *MNRAS*, 434, 2167
- Komatsu E. et al., 2011, *ApJS*, 192, 18
- Lavaux G., Wandelt B. D., 2010, *MNRAS*, 403, 1392
- Lavaux G., Wandelt B. D., 2012, *ApJ*, 754, 109
- Lavaux G., Mohayaee R., Colombi S., Tully R. B., Bernardeau F., Silk J., 2008, *MNRAS*, 383, 1292
- Lee J., Park D., 2006, *ApJ*, 652, 1
- Li B., Zhao H., 2009, *Phys. Rev. D*, 80, 044027
- Li B., Zhao G.-B., Koyama K., 2012, *MNRAS*, 421, 3481
- Manera M. et al., 2013, *MNRAS*, 428, 1036
- Neyrinck M. C., 2008, *MNRAS*, 386, 2101
- Neyrinck M. C., Falck B. L., Szalay A. S., 2013, preprint ([arXiv:1309.4787](https://arxiv.org/abs/1309.4787))
- Padilla N. D., Ceccarelli L., Lambas D. G., 2005, *MNRAS*, 363, 977
- Pan D. C., Vogeley M. S., Hoyle F., Choi Y.-Y., Park C., 2012, *MNRAS*, 421, 926
- Pápai P., Szapudi I., Granett B. R., 2011, *ApJ*, 732, 27
- Paranjape A., Lam T. Y., Sheth R. K., 2012, *MNRAS*, 420, 1648
- Park D., Lee J., 2007, *ApJ*, 665, 96
- Pisani A., Lavaux G., Sutter P. M., Wandelt B. D., 2013, preprint ([arXiv:1306.3052](https://arxiv.org/abs/1306.3052))
- Planck Collaboration, 2013, preprint ([arXiv:1303.5079](https://arxiv.org/abs/1303.5079))
- Platen E., van de Weygaert R., Jones B. J. T., 2007, *MNRAS*, 380, 551
- Quinn T., Katz N., Stadel J., Lake G., 1997, preprint ([astro-ph/9710043](https://arxiv.org/abs/astro-ph/9710043))
- Ricciardelli E., Quilis V., Varela J., 2014, *MNRAS*, 440, 601
- Ryden B. S., 1995, *ApJ*, 452, 25
- Ryden B. S., Melott A. L., 1996, *ApJ*, 470, 160
- Schmidt J. D., Ryden B. S., Melott A. L., 2001, *ApJ*, 546, 609
- Sheth R. K., van de Weygaert R., 2004, *MNRAS*, 350, 517 (SVdW)
- Shoji M., Lee J., 2012, preprint ([arXiv:e-prints](https://arxiv.org/abs/e-prints))
- Spolyar D., Sahlén M., Silk J., 2013, preprint ([arXiv:e-prints](https://arxiv.org/abs/e-prints))
- Strauss M. A. et al., 2002, *AJ*, 124, 1810
- Sutter P. M., Lavaux G., Wandelt B. D., Weinberg D. H., 2012a, *ApJ*, 761, 44
- Sutter P. M., Lavaux G., Wandelt B. D., Weinberg D. H., 2012b, *ApJ*, 761, 187
- Sutter P. M., Lavaux G., Wandelt B. D., Weinberg D. H., Warren M. S., 2013, preprint ([arXiv:1310.7155](https://arxiv.org/abs/1310.7155))
- Sutter P. M., Lavaux G., Wandelt B. D., Weinberg D. H., Warren M. S., 2014, *MNRAS*, 438, 3177
- Tavasoli S., Vasei K., Mohayaee R., 2013, *A&A*, 553, A15
- Taylor A. M., Vovk I., Neronov A., 2011, *A&A*, 529, A144
- Thompson L. A., Gregory S. A., 2011, preprint ([arXiv:1109.1268](https://arxiv.org/abs/1109.1268))
- Thompson K. L., Vishniac E. T., 1987, *ApJ*, 313, 517
- Tinker J. L., Conroy C., 2009, *ApJ*, 691, 633
- Tinker J. L., Weinberg D. H., Zheng Z., 2006, *MNRAS*, 368, 85
- Warren M. S., 2013, SC '13: Proc. Int. Conf. on High Performance Computing, Networking, Storage and Analysis, preprint ([arXiv:1310.4502](https://arxiv.org/abs/1310.4502))
- Watson W. A., Iliev I. T., Diego J. M., Gottlöber S., Knebe A., Martínez-González E., Yepes G., 2014, *MNRAS*, 437, 3776
- Zehavi I. et al., 2011, *ApJ*, 736, 59
- Zheng Z., Coil A. L., Zehavi I., 2007, *ApJ*, 667, 760

This paper has been typeset from a  $\text{\TeX}/\text{\LaTeX}$  file prepared by the author.